ACS Catalysis

pubs.acs.org/acscatalysis Letter

Keep the Ligands: Potential Benefits for Fuel Cell Performance

Andrés Molina Villarino,[‡] Jonathan L. Rowell,[‡] Dasol Yoon, Qihao Li, Yafu Jia, Zixiao Shi, Joesene Soto, Julia Koldobskiy, David A. Muller, Richard D. Robinson,* and Héctor D. Abruña*

Cite This: ACS Catal. 2024, 14, 5436−5443 Read Online

ACCESS | Metrics & More | Article Recommendations | Supporting Information

ABSTRACT: Spinel oxides such as ternary cobalt manganese spinel oxides (CMOs) are promising electrocatalysts for oxygen reduction reaction (ORR) in anion exchange membrane fuel cells. Current efforts to enhance fuel cell cathode performance predominantly focus on tuning the ORR activity through the chemical and crystallographic engineering of the active material. However, the impact of ink formulation and film homogeneity on fuel cell performance remains poorly understood and under-investigated. Here we show that the deliberate retention of organic ligands can enhance the performance of a CMO/C composite by improving its film homogeneity. Surprisingly, retaining the organic ligands can optimize the catalyst−ionomer affinity and subsequent film homogeneity of this system, thus enhancing its fuel cell peak power density from 0.8 W/cm^2 to 1.2 W/cm^2. We demonstrate this effect by pre- and postsynthetic characterizations of single-batch and monodisperse CMO/C composites and films, in the presence (retained) and absence (removed) of organic ligands. Our results demonstrate that ink dispersion and film homogeneity are critical parameters in fuel cell electrocatalysis and how organic ligands can help enhance electrocatalytic film performance in systems that suffer from unfavorable electrocatalyst−ionomer interactions.

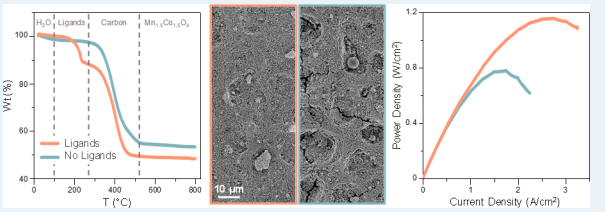

KEYWORDS: *electrocatalysis, fuel cell, membrane electrode assembly, oxygen reduction reaction, colloidal nanoparticles*

Fuel cells convert hydrogen and oxygen into water and electricity at efficiencies much higher than those of an internal combustion engine.[1] These will eventually be needed to meet global energy demands. In order to operate, they require highly active and stable oxygen reduction reaction (ORR) electrocatalysts to enable high current densities and peak power densities at operating temperatures (<80 °C).[2] While state-of-the-art electrocatalysts are typically derived from platinum group metals (PGMs),[3] recent articles show the promise of nonprecious metal electrocatalysts, especially in alkaline media, including cobalt−manganese oxide (CMO) spinel,[4−6] metal−organic framework (MOF)-derived nanoparticles,[7] single Cu atom and Cu cluster-anchored nitrogen-doped carbons,[8] Co-functionalized reduced graphene oxides,[9] and MnO-modified Co−N$_x$ particles.[10] The traditional route to electrocatalyst optimization has been to modify the chemical composition, surface strain, and/or other properties exclusive to the active material within the catalyst.[3,9,11−17] Seldom are factors such as ink formulation and/or resulting film homogeneity systematically studied and optimized for high performance using new electrocatalysts. Attempts to understand the effects of film homogeneity are usually limited to Pt/C systems,[18] and ink and film making methods and conditions can vary greatly from group to group; and sometimes even within groups. Furthermore, the effect of ionomer−catalyst interactions is likely very different for metal oxide catalyst compared to traditional PGM catalysts. The surfaces of metal-oxide catalysts are dominated by polar hydroxyl groups, whereas the surfaces of PGM catalysts are usually nonpolar and metallic in nature. Unraveling how catalyst−ionomer interactions affect film homogeneity and performance is critical to the use of non-PGM electrocatalysts going forward. A key unknown in electrocatalytic films from nanomaterials is how much the electrocatalyst film homogeneity influences the electrocatalyst performance. Disentanglement of catalyst activity and film homogeneity could lead to advanced optimization protocols and a better understanding of catalytic mechanisms and thus to the widespread application of new nonprecious metal electrocatalysts in high performance fuel cells and related applications and technologies.

Here, we approach this challenge by optimizing a known and promising cobalt−manganese oxide (CMO) spinel electrocatalyst (i.e., $Co_{1.5}Mn_{1.5}O_4$)[19,20] using an unconventional approach. Organic ligands used in colloidal nanocrystal syntheses of electrocatalysts are usually removed prior to electrochemical performance tests, as per conventional wisdom in the field.[5] This step is intended to make electrocatalyst active sites accessible to reactants and lower the film resistivity.

Received: December 26, 2023
Revised: March 20, 2024
Accepted: March 21, 2024
Published: March 27, 2024

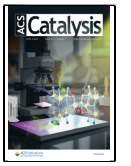

https://doi.org/10.1021/acscatal.3c06298
ACS Catal. 2024, 14, 5436−5443

However, this step can have enormous effects on the nanocrystal dispersibility and electrocatalyst film homogeneity. In this work we, instead, retained the nanocrystal organic ligand capping agents of lauric acid ($HOOC_{12}H_{23}$) and octylamine ($H_2NC_8H_{17}$) throughout the ink dispersion and film deposition steps, and produced a much more uniform and active fuel cell cathode film. When directly comparing ligand-capped and ligand-free $Co_{1.43}Mn_{1.57}O_4$/C composites made from a single large-scale batch (~1.4 g) colloidal synthesis, the ligand-capped composite outperformed (by a factor of 1.5) the ligand-free composite in a single-stack fuel cell. We ascribe this increase in performance to lower ionic resistance from the more homogeneous catalyst films that result from the use of ligand capped particles during film processing.

RESULTS AND DISCUSSION

Our recently developed synthesis[19] uses octylamine as a reagent, solvent, and surface capping ligand to produce small, monodisperse (6 ± 2 nm), and colloidally stable $Co_{1.43}Mn_{1.57}O_4$ nanocrystals. Compared to previous reports, this strategy pushes the limits of homogeneity and atom utilization for CMO spinel electrocatalysts.[5,6,21] Synthesizing the nanocrystals through a low-temperature colloidal heat-up method,[22] as opposed to hydrothermal[23] or other high-temperature/pressure strategies,[24,25] not only provides a tighter size distribution and prevents aggregation, but allows for the decoupling of composite formation from the nanocrystal synthesis. This two-step approach allows for the systematic study of same-batch nanocrystals with different supports or additives.

Transmission electron microscopy (TEM) images of our ligand-capped nanocrystals show multimicron superlattices on TEM grids, due to their monodispersity (Figure 1a). The nanocrystals also form homogeneously distributed composites when loaded on a carbon support (Figure 1b), with tunable composite mass loadings of up to about 70%. Scanning transmission electron microscopy (STEM) images and energy dispersive X-ray spectroscopy (EDS) elemental maps show that the CMO nanocrystals exhibit a spinel crystal structure (Figure 1c) and a Mn-rich core (Figure 1d). The observed nanocrystal superlattice assembly is consistent with an estimated monolayer surface coverage[26] of organic ligands (Figure S1).

We found 15 h of annealing in air at 175 °C to be an optimal ligand removal strategy for the CMO/C system (Figure 2a, b). Lower temperatures and longer annealing times serve to remove virtually all of the ligands[2] without dramatically increasing the particle size (6.4 to 6.7 nm) or causing support aggregation (Figures S2 and S7). Thermogravimetric analyses (TGA) for ligand-capped and ligand-free powders are shown in Figure 2b. Water desorption—or its absence—at the beginning of the profiles evidence the hydrophilic and hydrophobic nature of the two different/distinct surfaces.[27] This change in surface hydrophobicity is likely particular to metal-oxide nanocrystals due to their ligand-free surfaces being dominated by polar hydroxyl groups. This is unlike the case for the more commonly used PGM nanocrystal electrocatalysts, whose surfaces remain hydrophobic after ligand removal. Ligand content, by mass, corresponds to approximately 10 and 0 wt % (Figure S2a, b) for ligand-capped and ligand-free CMO, respectively. Carbon support decomposition is slightly different for ligand-free samples, as a result of surface chemistry.[28] The net increase in composite mass loading

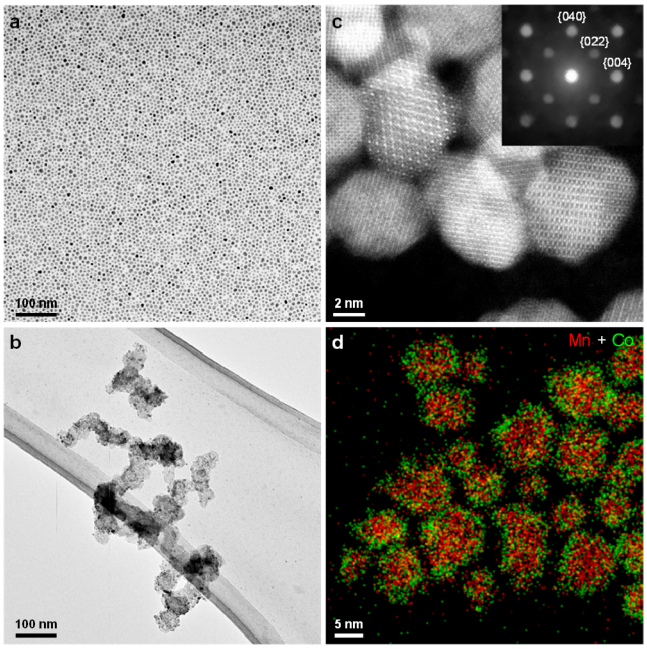

Figure 1. Physical characterization of CMO/C nanostructure. (a) TEM of micron-size superlattice composed of ligand-capped CMO nanocrystals. (b) TEM of ligand-capped CMO/C (loaded on Ketjenblack carbon support). (c) HAADF STEM of ligand-free CMO nanocrystals. Inset shows the nanobeam electron diffraction pattern of a spinel nanocrystal oriented along the [100] zone axis. (d) EDS elemental map of ligand-free CMO nanocrystals.

(i.e., CMO vs total mass) after ligand removal is about 5 wt %, which makes our samples comparable for electrocatalysis.

Powder X-ray diffraction (XRD) for ligand-capped and ligand-free powders indicates that the number, relative intensity, and full width at half-maximum (fwhm) of diffraction peaks are virtually identical, demonstrating that the CMO nanocrystals retain their spinel crystal structure and size after ligand removal (Figure 2c). A small lattice contraction of 0.7 ± 0.3% (Figure S3) for ligand-free CMO is consistent with the electron-donating and charge-passivating behavior of organic ligands[29] such as octylamine or lauric acid. In short, low-temperature ligand removal does not significantly alter the crystal structure of the CMO spinels.

X-ray photoelectron spectroscopy (XPS) for ligand-capped and ligand-free CMO shows no substantial differences in peak shape in the Co and Mn 2p spectra (Figure 2d, e), indicating that the chemical environments around the metal centers remain virtually unchanged after ligand removal. However, there are small (<0.2 eV) shifts in the binding energies for both Co and Mn after ligand removal that suggest that the electronic density of the metal centers is slightly different, with Mn experiencing a higher relative oxidation state. This observation is consistent with the lattice contraction discussed above. The O 1s spectra (Figure 2f) for ligand-capped CMO exhibit a significant contribution from the higher binding energy component (ca. 532 eV), which we ascribe to the metal−ligand oxygen bond (M−O−L).[30] This M−O−L peak is absent for ligand-free CMO. This change in the surface oxygen after heat treatment further confirms the effective removal of ligands from the surface of the CMO nanocrystals after annealing in air. Moreover, the C 1s spectra (Figure 2g) are identical for ligand-capped and ligand-free CMO, as both are still ~50 wt % high-surface area carbon. Overall, while our

https://doi.org/10.1021/acscatal.3c06298
ACS Catal. 2024, 14, 5436−5443

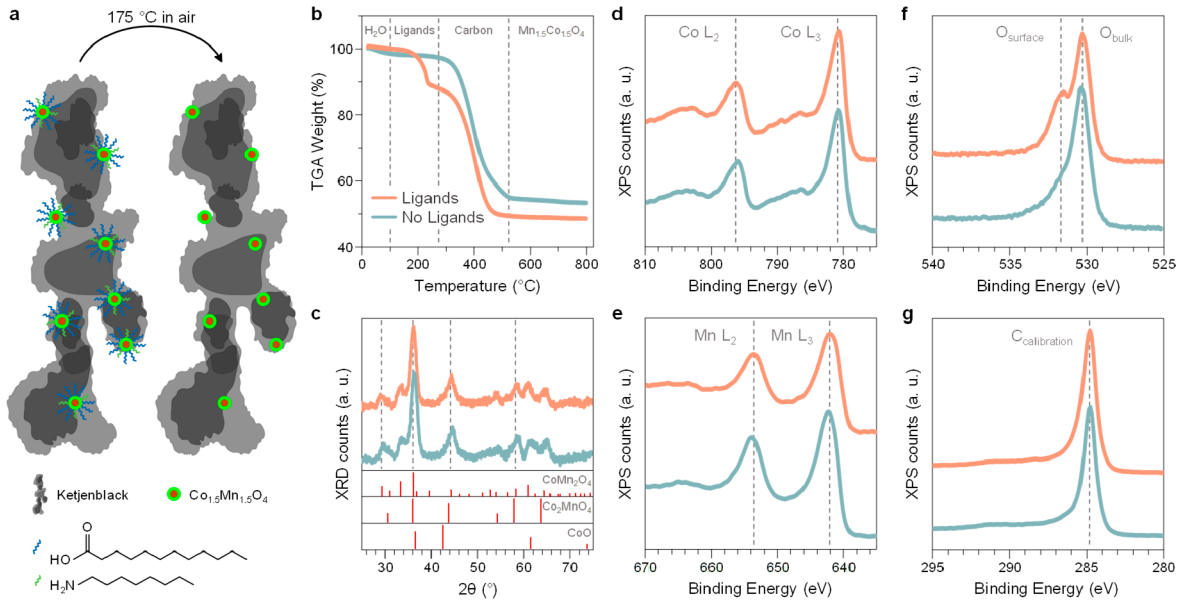

Figure 2. Organic ligand removal strategy and physical characterization of CMO/C powders. (a) Schematic showing the one-step ligand removal strategy used in this study. (b) TGA of CMO/C before and after ligand removal. Dotted lines separate the four main thermal stability regions, which include one desorption process, two decomposition processes, and a stable window. (c) Powder XRD of CMO/C before and after ligand removal. Dotted lines highlight the (112), (211), (220), and (321) diffraction planes of the $CoMn_2O_4$ spinel reference, from left to right. (d–g) XPS of CMO/C before and after ligand removal. Dotted lines highlight the main peaks observed. Colors correspond to the labels in (b).

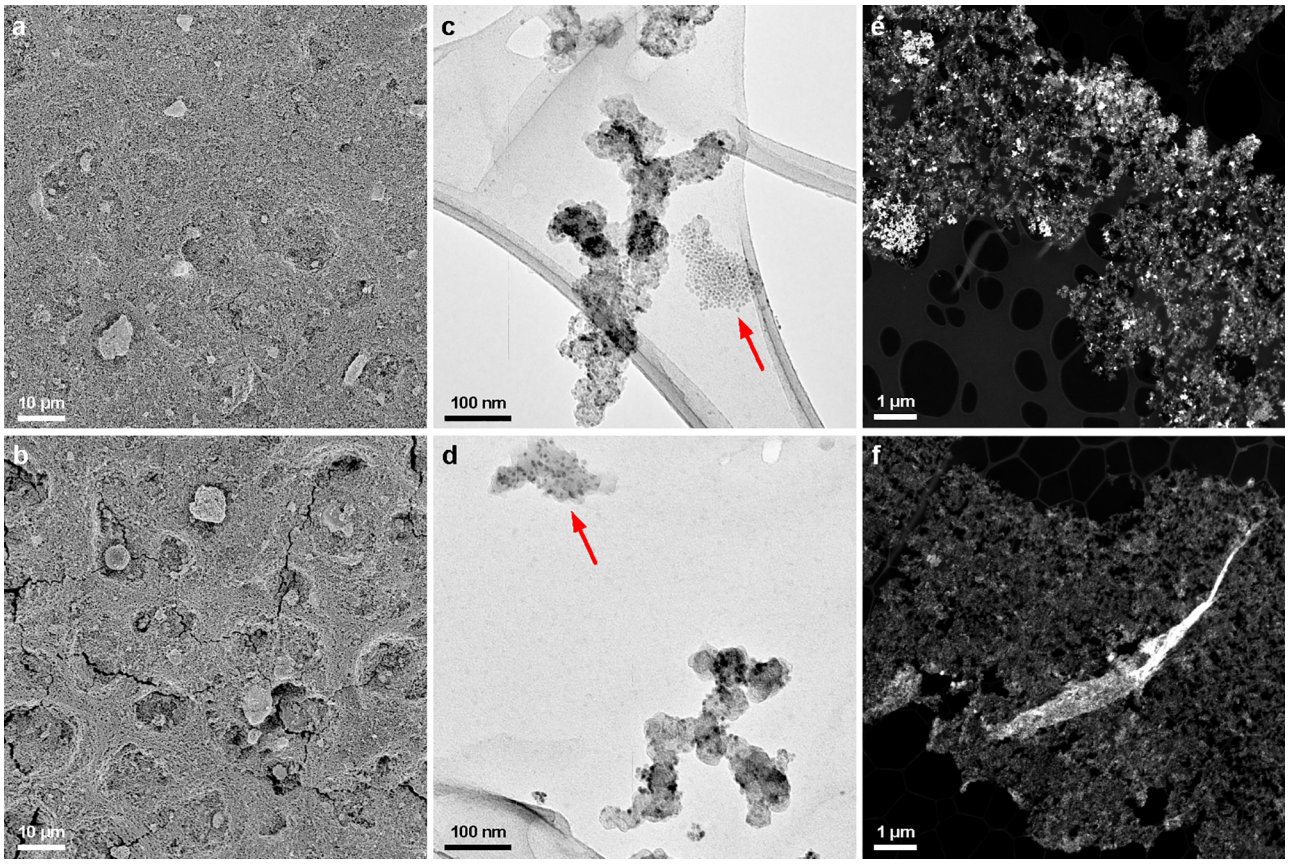

Figure 3. Micro- and nanostructure uniformity effects of organic ligands on CMO/C/QAPPT inks and films. All top panels correspond to ligand-capped CMO/C/QAPPT, and all bottom panels correspond to ligand-free CMO/C/QAPPT. (a, b) SEM of MEA films of ligand-capped (a) and ligand-free (b) CMO/C/QAPPT cathodes. (c, d) TEM of ligand-capped (c) and ligand-free (d) CMO/C/QAPPT. Red arrows point at the superlattices (c) and nanocrystal-ionomer clusters (d) of CMO/C/QAPPT before and after ligand removal. (e, f) HAADF STEM of microtomed MEA films of ligand-capped (e) and ligand-free (f) CMO/C/QAPPT cathodes.

https://doi.org/10.1021/acscatal.3c06298
ACS Catal. 2024, 14, 5436−5443

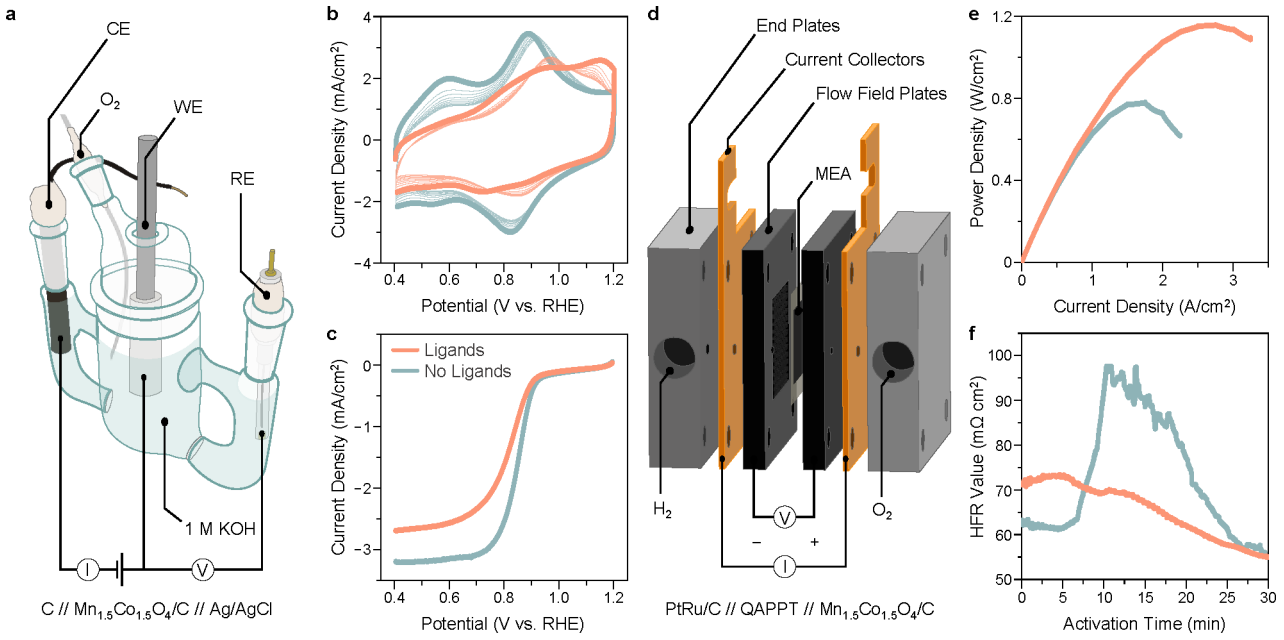

Figure 4. Electrochemical cell and fuel cell performance effects of organic ligands on CMO/C/QAPPT cathodes. (a) Schematic demonstrating the RDE technique. The cell is filled with Ar- or O_2-saturated 1 M KOH, and the working electrode is rotated at 1600 rpm. (b, c) CV of ligand-capped and ligand-free CMO/C/QAPPT in Ar-saturated (b) followed by O_2-saturated (c) 1 M KOH at 50 mV/s and 5 mV/s, respectively. Lighter curves correspond to subsequent cycles. (d) Schematic demonstrating the fuel cell device, including the three-layer MEA. The gaskets electronically insulating the two flow field plates and the flow field plate voltage and current leads are omitted for clarity. (e, f) MEA device power density (e) and high frequency resistance (HFR) (f) of ligand-capped and ligand-free CMO/C/QAPPT with testing conditions of 80 °C, 200 kPa backpressure, and 1500 sccm H_2/O_2. Colors correspond to the labels in (c).

ligand removal strategy does not appear to alter the bulk crystal structure or chemical environment of CMO, it drastically changes the CMO surface chemistry.

We investigated the effects of electrocatalyst surface chemistry on fuel cell ink formulation and subsequent film homogeneity using quaternary ammonium poly(*N*-methylpiperidine-*co*-*p*-terphenyl) (QAPPT) alkaline polymer electrolytes as anion-exchange membrane fuel cell (AEMFC) membrane and ionomer. We compared catalyst inks and postelectrochemical test membrane electrode assembly (MEA) catalyst films, which exhibit significant differences. Notably, scanning electron microscopy (SEM) images for ligand-capped and ligand-free CMO/C cathode layers containing QAPPT exhibit clear differences in terms of film homogeneity (Figure 3a, b). Ligand-capped CMO/C films are significantly more uniform and smoother than ligand-free CMO/C films, with the latter showing a large number and density of cracks. These differences are observed over thousands of squared micrometers (Figure S4a–f). To ensure these effects were not due to variations in deposition or film thickness, we measured the thickness range for each layer of the MEA for 3 SEM images per sample. We found that the thicknesses ranges for the ligand and no ligand samples were very similar, with the anodes ranging from 3.9 to 10 μm, the cathodes 7.5–14.2 μm, and the electrolytes 14.9–18.3 μm (Table S1). In addition, as shown in Figure S10, the ligand capped nanoparticles were clearly better dispersed in the ionomer solution than the ligand-free sample before sonication. This difference in dispersion quality likely leads to the observed differences of the resulting films. However, following sonication, the two samples appeared so dark that they could no longer be differentiated. After almost a week, neither sample had any visible precipitate. Since the catalyst layers are essentially identical in thickness (Figure S4g, h), the observed differences correspond to the interactions within the cathode films themselves, and not between the films and the membrane.[31] Additionally, the poor film homogeneity of ligand-free samples cannot be explained by thermal annealing-induced aggregates of the composite, as evidenced by the larger Brunauer–Emmett–Teller (BET) surface area[32] they exhibit (Figure S2e).

TEM images for ligand-capped and ligand-free CMO/C inks containing QAPPT also show notable differences in homogeneity (Figures 3c, d and S5). While ligand removal barely affects the average CMO spinel nanocrystal size distribution (Figure S2c, d), it allowed for the formation of ionomer-nanocrystal clusters (Figure 3d). These ionomer-nanocrystal clusters (Figure S5) are not observed in ligand-capped CMO/C, which exhibit short-range superlattices of nanocrystals instead (Figure 3c). The average particle size, for both the ligand-capped and the ligand-free MEA inks, was not significantly impacted by the addition of ionomer, with both averaging 6.5 nm (from TEM measurements of over 200 particles) (Figure S11). Overall, ligand removal transforms the CMO nanocrystal surface chemistry from hydrophobic to hydrophilic, significantly enhancing the wettability of CMO by the ionomer.[33,34] This leads to the ionomer aggregating around the ligand removed nanocrystals, decreasing the homogeneity of the film. In other words, retaining the organic ligands keeps the CMO surface hydrophobic and prevents excessive wettability of the CMO by the ionomer, thus greatly enhancing ink and film homogeneity and, subsequently, film performance. This finding is likely specific to metal-oxide catalysts because when the ligands are removed, the surfaces will be covered by polar hydroxyl groups, making them very hydrophilic. PGM electrocatalysts retain their nonpolar surfaces after thermal removal of the ligands.

https://doi.org/10.1021/acscatal.3c06298
ACS Catal. 2024, 14, 5436–5443

Low-magnification STEM images of microtomed post-mortem CMO/C/QAPPT MEA films further evidence the differences in film homogeneity (Figure 3e, f). While ligand-capped CMO/C/QAPPT shows a more homogeneous distribution of spinel nanocrystals (Figure 3e), ligand-free CMO/C/QAPPT is characterized by localized strips of clustered nanocrystals, as shown in the center of the image (Figure 3f). These clusters are assumed to strain the film and cause the large cracks observed in the SEM images (Figure 3b). Thus, ligand removal affects the CMO nanocrystal surface chemistry and subsequent film homogeneity, critically affecting the electrode film homogeneity.

To assess the effects of ink and film homogeneity on the electrocatalytic activity and fuel cell performance of our CMO/C composites, we used rotating disk electrode (RDE) voltammetry and MEA measurements. The experimental setups are shown in Figure 4a, d, and all voltages are referenced against the reversible hydrogen electrode (RHE).

Electrochemical tests performed using single-batch ligand-capped and ligand-free CMO films drop cast on a glassy carbon RDE (Figure 4a) reveal several critical differences in the electrochemical response (Figure 4b, c). Ligand-capped CMO films exhibit a more resistive behavior in both Ar- and O_2-saturated electrolytes, typical of ligand-blocked active sites and stray resistance.[35] Only ligand-capped CMO films undergo additional oxidation around +1.1 V vs RHE in an Ar-saturated electrolyte (Figure 4b), which we ascribe to the oxidative desorption of the ligands. Though we considered electrochemical methods to remove the ligands,[35] we feared that cycling to high potentials would likely alter the spinel crystal structure,[36] which would, in turn, complicate comparisons of the observed electrochemical responses. Similarly, electrochemical window opening experiments showed a decrease in current density and significant shifts in potential for the main redox peaks in the voltammetric profile when the potential was cycled below +0.5 vs RHE (Figure S8), and so cycling to potentials below −0.1 V vs RHE would most certainly also cause a phase transformation and/or degradation of the catalyst. Ligand-capped CMO films also exhibit multiple isopotential points (Figure 4b), typical of surface transformations at a constant surface coverage as a function of time. Ligand-free CMO films exhibit significantly more well-defined spinel features compared with ligand-capped CMO (Figure 4b). In addition, ligand-capped CMO films exhibit a significantly higher formal redox potential ($E^{\circ\prime}$) for the main redox process around +0.9 V vs RHE when compared to ligand-free CMO, with a larger peak separation (ΔE_p). Although this difference in $E^{\circ\prime}$ would suggest[8,21] that ligand-capped CMO should be more active toward the ORR, we find that ORR activity for the same CMO films (Figure 4c) follows the opposite trend in terms of onset potential (E_{onset}), half-wave potential ($E_{1/2}$), and diffusion-limited current (j_L). Thus, our observations are in contrast with previous hypotheses regarding CMO spinel redox potential coupling to ORR catalysis.[8,21] Taken in isolation, these RDE results would suggest that ligands, in fact, hinder electrocatalytic performance and should therefore be removed prior to practical applications.[37] However, our fuel cell results clearly indicate otherwise.

Fuel cell tests performed using single-batch ligand-capped and ligand-free CMO cathode films on QAPPT membranes are shown in Figure 4e, f. In both current density and power density, ligand-capped CMO outperforms the ligand-free counterpart by a factor of 1.5, with the former reaching an extraordinary peak power density of 1.2 W/cm^2 (Figure 4e). Additionally, the MEA activation process of the ligand-free CMO films is quite erratic. This is evidenced by sudden increases in high frequency resistance (HFR), starting after a load is applied (Figure 4f). This increase in resistance was also borne-out in the $I-V$ curves for the MEAs, with the ligand-free sample clearly showing a steeper slope and reaching a significantly lower current density than the ligand-containing sample (Figure S9), likely indicating greater ohmic losses in the no ligands MEA. Since the HFR of a fuel cell MEA is an indirect measure of its ionic resistance,[38] ionic transport limitations are likely the cause for the marked differences in fuel cell performance between ligand-capped and ligand-free CMO cathodes. This difference in ionic resistance agrees well with the observed differences in the film homogeneity. A composite with smaller, more evenly distributed conductive domains will have a higher overall conductivity than one with larger aggregated conductive domains, based on percolation theory.[39−41] In other words, ligand-capped CMO benefits from more favorable catalyst−ionomer interactions compared to ligand-free CMO, which results in a more homogeneous distribution of ionomer in the composite, ideal for the high ionic conductivity needed to achieve high power densities. Thus, appropriate catalyst−ionomer interactions are crucial when large loads are applied and ionic resistance dominates over kinetic barriers.[42] In this case, properties such as electrochemically active surface area (ECSA) can become secondary to favorable catalyst−ionomer interactions and network formation that enable and facilitate ionic transport. It should be noted that the testing conditions and fabrication of the fuel cell and MEAs are quite different from those employed in the RDE experiments. In short, after deposition, the MEAs are ion-exchanged to replace the halide counterion in the QAPPT with hydroxide. This is carried out by heating the films in 1 M NaOH at 70 °C for 48 h. Subsequently, the fuel cell tests are performed at 80 °C in an O_2 atmosphere. While we are not absolutely certain, we feel confident that under the conditions of elevated temperatures and highly alkaline environment, the ligands are likely displaced from the catalyst surface, and therefore, they do not affect/hinder catalyst activity. However, the ligand effects on film homogeneity remain since the MEA composite remains in the solid state after deposition/spraying.

In this work, a large-scale colloidal synthesis and a ligand removal strategy are used to compare organic ligand-capped and ligand-free small and monodisperse CMO/C composites as promising AEMFC ORR electrocatalysts. In the QAPPT polymer electrolyte system, ligand-capped CMO cathodes outperform their ligand-free counterparts in terms of peak power density by a factor of 1.5. This difference in performance is likely caused by the marked differences observed in the nanocrystal-ionomer interaction and wettability and subsequent catalyst film homogeneity resulting from ligand removal. Other physical properties, such as crystal structure, bulk chemical environment, and particle size, remained virtually unchanged after ligand removal. Further study of the observed phenomenon could significantly enhance the development of nonprecious metal oxides as practical electrocatalysts for anion exchange membrane fuel cells.

https://doi.org/10.1021/acscatal.3c06298
ACS Catal. 2024, 14, 5436−5443

■ ASSOCIATED CONTENT

Supporting Information

The Supporting Information is available free of charge at https://pubs.acs.org/doi/10.1021/acscatal.3c06298.

Additional calculations, TGA, BET analysis, size distributions, and microscopy (PDF)

■ AUTHOR INFORMATION

Corresponding Authors

Richard D. Robinson − *Department of Materials Science and Engineering and Kavli Institute at Cornell (KIC) for Nanoscale Science, Cornell University, Ithaca, New York 14853, United States of America;* orcid.org/0000-0002-0385-2925; Email: rdr82@cornell.edu

Héctor D. Abruña − *Department of Chemistry and Chemical Biology, Cornell University, Ithaca, New York 14853, United States of America;* orcid.org/0000-0002-3948-356X; Email: hda1@cornell.edu

Authors

Andrés Molina Villarino − *Department of Chemistry and Chemical Biology, Cornell University, Ithaca, New York 14853, United States of America;* orcid.org/0000-0003-3272-5156

Jonathan L. Rowell − *Department of Chemistry and Chemical Biology, Cornell University, Ithaca, New York 14853, United States of America;* orcid.org/0000-0002-2959-8638

Dasol Yoon − *Department of Materials Science and Engineering, Cornell University, Ithaca, New York 14853, United States of America;* orcid.org/0000-0003-2284-7010

Qihao Li − *Department of Chemistry and Chemical Biology, Cornell University, Ithaca, New York 14853, United States of America*

Yafu Jia − *Department of Materials Science and Engineering, Cornell University, Ithaca, New York 14853, United States of America*

Zixiao Shi − *Department of Chemistry and Chemical Biology, Cornell University, Ithaca, New York 14853, United States of America*

Joesene Soto − *Department of Chemistry and Chemical Biology, Cornell University, Ithaca, New York 14853, United States of America; Kavli Institute at Cornell (KIC) for Nanoscale Science, Cornell University, Ithaca, New York 14853, United States of America*

Julia Koldobskiy − *Department of Materials Science and Engineering, Cornell University, Ithaca, New York 14853, United States of America*

David A. Muller − *Kavli Institute at Cornell (KIC) for Nanoscale Science and School of Applied and Engineering Physics, Cornell University, Ithaca, New York 14853, United States of America;* orcid.org/0000-0003-4129-0473

Complete contact information is available at: https://pubs.acs.org/10.1021/acscatal.3c06298

Author Contributions

‡A.M.V. and J.L.R. contributed equally. A.M.V. and J.L.R. designed and led the project, contributing equally. A.M.V. designed and performed the physical (TGA, XRD, XPS, and low-magnification TEM) and electrochemical (RDE and MEA) characterizations and tests, aided by Q.L., J.S., and J.K. J.L.R. designed and performed the syntheses of the electrocatalysts used in this study, aided by Y.J. D.Y. and Z.S. performed the high-resolution STEM characterizations. D.A.M., R.D.R., and H.D.A. supervised the entirety of the project and provided intellectual guidance. All authors revised and approved the final version of the manuscript.

Notes

The authors declare no competing financial interest.

■ ACKNOWLEDGMENTS

A.M.V. acknowledges support by the National Science Foundation (NSF) Graduate Research Fellowship Program (GRFP) grant DGE-1650441 and DGE-2139899, and the Cornell Dean's Excellence Scholarship. J.L.R. acknowledges support by the Center for Alkaline Based Energy Solutions (CABES), an Energy Frontier Research Center funded by the U.S. Department of Energy (DOE), Office of Science, Basic Energy Sciences (BES), under Award # DE-SC0019445. Q.L. acknowledges support by the New York State Energy Research and Development Authority (NYSERDA) under agreement 146218. J.S. acknowledges support by the Cornell Energy Systems Institute (CESI) and the Kavli Institute at Cornell (KIC). R.D.R. acknowledges the donors of the American Chemical Society Petroleum Research Fund (ACS PRF) for partial support of this research. A special thanks go to Tatyana Dokuchayeva and Lyndsey Fisher for the ICP-AES and ICP-MS data acquisition, the Cornell Center for Materials Research (CCMR, DMR-1719875, NSF-MRI-1429155), CESI, and the Cornell Nutrient Analysis Laboratory (CNAL), and Mr. Krumov, Dr. Jeesoo Seok, Kelly Case, and Mengqi Duan for revising the manuscript.

■ ABBREVIATIONS

CMO	cobalt−manganese oxide
PGM	platinum group metal
ORR	oxygen reduction reaction
TEM	transmission electron microscopy
STEM	scanning transmission electron microscopy
EDS	energy dispersive X-ray spectroscopy
HAADF	high angle annular dark field
TGA	thermogravimetric analysis
XRD	X-ray diffraction
fwhm	full width at half-maximum
XPS	X-ray photoelectron spectroscopy
QAPPT	*N*-methylpiperidine-*co*-*p*-terphenyl
AEMFC	alkaline exchange membrane fuel cell
SEM	scanning electron microscopy
BET	Brunauer−Emmett−Teller
RDE	rotating-disk electrode
RHE	reversible hydrogen electrode
HFR	high-frequency resistance
MEA	membrane electrode assembly

■ REFERENCES

(1) Abdelkareem, M. A.; Elsaid, K.; Wilberforce, T.; Kamil, M.; Sayed, E. T.; Olabi, A. Environmental aspects of fuel cells: A review. *Science of The Total Environment* **2021**, *752*, 141803.

(2) Ferriday, T. B.; Middleton, P. H. Alkaline fuel cell technology - A review. *Int. J. Hydrogen Energy* **2021**, *46* (35), 18489−18510.

(3) Li, H.; Zeng, R.; Feng, X.; Wang, H.; Xu, W.; Lu, X.; Xie, Z.; Abruña, H. D. Oxidative Stability Matters: A Case Study of Palladium Hydride Nanosheets for Alkaline Fuel Cells. *J. Am. Chem. Soc.* **2022**, *144* (18), 8106−8114.

(4) Yang, Y.; Xiong, Y.; Holtz, M. E.; Feng, X.; Zeng, R.; Chen, G.; DiSalvo, F. J.; Muller, D. A.; Abruna, H. D. Octahedral spinel electrocatalysts for alkaline fuel cells. *Proc. Natl. Acad. Sci. U. S. A.* **2019**, *116* (49), 24425−24432.
(5) Kim, J.; Ko, W.; Yoo, J. M.; Paidi, V. K.; Jang, H. Y.; Shepit, M.; Lee, J.; Chang, H.; Lee, H. S.; Jo, J.; Kim, B. H.; Cho, S. P.; van Lierop, J.; Kim, D.; Lee, K. S.; Back, S.; Sung, Y. E.; Hyeon, T. Structural Insights into Multi-Metal Spinel Oxide Nanoparticles for Boosting Oxygen Reduction Electrocatalysis. *Adv. Mater.* **2022**, *34* (8), No. e2107868.
(6) Yang, Y.; Peng, H.; Xiong, Y.; Li, Q.; Lu, J.; Xiao, L.; DiSalvo, F. J.; Zhuang, L.; Abruña, H. D. High-Loading Composition-Tolerant Co−Mn Spinel Oxides with Performance beyond 1 W/cm^2 in Alkaline Polymer Electrolyte Fuel Cells. *ACS Energy Lett.* **2019**, *4* (6), 1251−1257.
(7) Liu, Z.; Ye, D.; Zhu, X.; Wang, S.; Zou, Y.; Lan, L.; Chen, R.; Yang, Y.; Liao, Q. ZIF-67-derived Co nanoparticles embedded in N-doped porous carbon composite interconnected by MWCNTs as highly efficient ORR electrocatalysts for a flexible direct formate fuel cell. *Chem. Eng. J.* **2022**, *432*, 134192.
(8) Yang, Z.; Jiang, K.; Tong, G.; Ke, C.; Wu, H.; Liu, P.; Zhang, J.; Ji, H.; Zhu, J.; Lu, C.; Zhuang, X. Copper-involved highly efficient oxygen reduction reaction in both alkaline and acidic media. *Chem. Eng. J.* **2022**, *437*, 135377.
(9) Yang, B.; Li, X.; Cheng, Q.; Jia, X.; Liu, Y.; Xiang, Z. A highly efficient axial coordinated CoN5 electrocatalyst via pyrolysis-free strategy for alkaline polymer electrolyte fuel cells. *Nano Energy* **2022**, *101*, 107565.
(10) Chen, C.; Tang, Z.-J.; Li, J.-Y.; Du, C.-Y.; Ouyang, T.; Xiao, K.; Liu, Z.-Q. MnO Enabling Highly Efficient and Stable Co-Nx/C for Oxygen Reduction Reaction in both Acidic and Alkaline Media. *Adv. Funct. Mater.* **2023**, *33* (1), 2210143.
(11) Zamora Zeledón, J. A.; Stevens, M. B.; Gunasooriya, G.; Gallo, A.; Landers, A. T.; Kreider, M. E.; Hahn, C.; Nørskov, J. K.; Jaramillo, T. F. Tuning the electronic structure of Ag-Pd alloys to enhance performance for alkaline oxygen reduction. *Nat. Commun.* **2021**, *12* (1), 620.
(12) Gao, R.; Wang, J.; Huang, Z.-F.; Zhang, R.; Wang, W.; Pan, L.; Zhang, J.; Zhu, W.; Zhang, X.; Shi, C.; Lim, J.; Zou, J.-J. Pt/Fe2O3 with Pt−Fe pair sites as a catalyst for oxygen reduction with ultralow Pt loading. *Nature Energy* **2021**, *6* (6), 614−623.
(13) Zeng, R.; Yang, Y.; Feng, X.; Li, H.; Gibbs, L. M.; DiSalvo, F. J.; Abruña, H. D. Nonprecious transition metal nitrides as efficient oxygen reduction electrocatalysts for alkaline fuel cells. *Science Advances* **2022**, *8* (5), No. eabj1584.
(14) Wang, Y.; Yang, Y.; Jia, S.; Wang, X.; Lyu, K.; Peng, Y.; Zheng, H.; Wei, X.; Ren, H.; Xiao, L.; Wang, J.; Muller, D. A.; Abruna, H. D.; Hwang, B. J.; Lu, J.; Zhuang, L. Synergistic Mn-Co catalyst outperforms Pt on high-rate oxygen reduction for alkaline polymer electrolyte fuel cells. *Nat. Commun.* **2019**, *10* (1), 1506.
(15) Yang, Y.; Wang, Y.; Xiong, Y.; Huang, X.; Shen, L.; Huang, R.; Wang, H.; Pastore, J. P.; Yu, S.-H.; Xiao, L.; Brock, J. D.; Zhuang, L.; Abruña, H. D. In Situ X-ray Absorption Spectroscopy of a Synergistic Co−Mn Oxide Catalyst for the Oxygen Reduction Reaction. *J. Am. Chem. Soc.* **2019**, *141* (4), 1463−1466.
(16) Yang, Z.; Wang, Y.; Zhu, M.; Li, Z.; Chen, W.; Wei, W.; Yuan, T.; Qu, Y.; Xu, Q.; Zhao, C.; Wang, X.; Li, P.; Li, Y.; Wu, Y.; Li, Y. Boosting Oxygen Reduction Catalysis with Fe−N4 Sites Decorated Porous Carbons toward Fuel Cells. *ACS Catal.* **2019**, *9* (3), 2158−2163.
(17) Li, X.; Li, X.; Liu, C.; Huang, H.; Gao, P.; Ahmad, F.; Luo, L.; Ye, Y.; Geng, Z.; Wang, G.; Si, R.; Ma, C.; Yang, J.; Zeng, J. Atomic-Level Construction of Tensile-Strained PdFe Alloy Surface toward Highly Efficient Oxygen Reduction Electrocatalysis. *Nano Lett.* **2020**, *20* (2), 1403−1409.
(18) Garsany, Y.; Singer, I. L.; Swider-Lyons, K. E. Impact of film drying procedures on RDE characterization of Pt/VC electrocatalysts. *J. Electroanal. Chem.* **2011**, *662* (2), 396−406.
(19) Rowell, J. L.; Jia, Y.; Shi, Z.; Molina Villarino, A.; Kang, M.; Yoon, D.; Jiang, K. Z.; Abruña, H. D.; Muller, D. A.; Robinson, R. D. General Route to Colloidally Stable, Low-Dispersity Manganese-Based Ternary Spinel Oxide Nanocrystals. *J. Am. Chem. Soc.* **2023**, *145* (31), 17406−17419.
(20) Perera, S. D.; Ding, X.; Bhargava, A.; Hovden, R.; Nelson, A.; Kourkoutis, L. F.; Robinson, R. D. Enhanced Supercapacitor Performance for Equal Co−Mn Stoichiometry in Colloidal $Co_{3-x}Mn_xO_4$ Nanoparticles, in Additive-Free Electrodes. *Chem. Mater.* **2015**, *27* (23), 7861−7873.
(21) Xiong, Y.; Yang, Y.; Feng, X.; DiSalvo, F. J.; Abruña, H. D. A Strategy for Increasing the Efficiency of the Oxygen Reduction Reaction in Mn-Doped Cobalt Ferrites. *J. Am. Chem. Soc.* **2019**, *141* (10), 4412−4421.
(22) Williamson, C. B.; Nevers, D. R.; Hanrath, T.; Robinson, R. D. Prodigious Effects of Concentration Intensification on Nanoparticle Synthesis: A High-Quality, Scalable Approach. *J. Am. Chem. Soc.* **2015**, *137* (50), 15843−15851.
(23) Sugioka, K.-i.; Ozawa, K.; Kubo, M.; Tsukada, T.; Takami, S.; Adschiri, T.; Sugimoto, K.; Takenaka, N.; Saito, Y. Relationship between size distribution of synthesized nanoparticles and flow and thermal fields in a flow-type reactor for supercritical hydrothermal synthesis. *Journal of Supercritical Fluids* **2016**, *109*, 43−50.
(24) Cheng, X.; Yan, P.; Liu, S.; Qian, M.; Wang, B.; Wan, Z.; Tian, J.; Shen, X.-C.; Isimjan, T. T.; Yang, X. Well-dispersed iron oxide stabilized FeN4 active sites in porous N-doped carbon spheres as alternative superior catalyst for oxygen reduction. *Int. J. Hydrogen Energy* **2019**, *44* (23), 12127−12137.
(25) Murray, C. B.; Norris, D. J.; Bawendi, M. G. Synthesis and characterization of nearly monodisperse CdE (E = sulfur, selenium, tellurium) semiconductor nanocrystallites. *J. Am. Chem. Soc.* **1993**, *115* (19), 8706−8715.
(26) Patil, V.; Mayya, K. S.; Pradhan, S. D.; Sastry, M. Evidence for Novel Interdigitated Bilayer Formation of Fatty Acids during Three-Dimensional Self-Assembly on Silver Colloidal Particles. *J. Am. Chem. Soc.* **1997**, *119* (39), 9281−9282.
(27) Okoye-Chine, C. G.; Moyo, M.; Hildebrandt, D. The effect of hydrophobicity on SiO2−supported Co catalysts in Fischer−Tropsch synthesis. *Fuel* **2021**, *296*, 120667.
(28) Sellin, R.; Clacens, J.-M.; Coutanceau, C. A thermogravimetric analysis/mass spectroscopy study of the thermal and chemical stability of carbon in the Pt/C catalytic system. *Carbon* **2010**, *48* (8), 2244−2254.
(29) Zanchet, D.; Tolentino, H.; Martins Alves, M. C.; Alves, O. L.; Ugarte, D. Inter-atomic distance contraction in thiol-passivated gold nanoparticles. *Chem. Phys. Lett.* **2000**, *323* (1), 167−172.
(30) Wilson, D.; Langell, M. A. XPS analysis of oleylamine/oleic acid capped Fe3O4 nanoparticles as a function of temperature. *Appl. Surf. Sci.* **2014**, *303*, 6−13.
(31) Tavassoli, A.; Lim, C.; Kolodziej, J.; Lauritzen, M.; Knights, S.; Wang, G. G.; Kjeang, E. Effect of catalyst layer defects on local membrane degradation in polymer electrolyte fuel cells. *J. Power Sources* **2016**, *322*, 17−25.
(32) Holade, Y.; Morais, C.; Servat, K.; Napporn, T. W.; Kokoh, K. B. Enhancing the available specific surface area of carbon supports to boost the electroactivity of nanostructured Pt catalysts. *Phys. Chem. Chem. Phys.* **2014**, *16* (46), 25609−25620.
(33) Wang, M.; Park, J. H.; Kabir, S.; Neyerlin, K. C.; Kariuki, N. N.; Lv, H.; Stamenkovic, V. R.; Myers, D. J.; Ulsh, M.; Mauger, S. A. Impact of Catalyst Ink Dispersing Methodology on Fuel Cell Performance Using in-Situ X-ray Scattering. *ACS Appl. Energy Mater.* **2019**, *2* (9), 6417−6427.
(34) Li, C.; Yu, K.; Bird, A.; Guo, F.; Ilavsky, J.; Liu, Y.; Cullen, D. A.; Kusoglu, A.; Weber, A. Z.; Ferreira, P. J.; Xie, J. Unraveling the Core of Fuel Cell Performance: Engineering the Ionomer/Catalyst Interface. *Energy Environ. Sci.* **2023**, *16*, 2977.
(35) Lu, L.; Lou, B.; Zou, S.; Kobayashi, H.; Liu, J.; Xiao, L.; Fan, J. Robust Removal of Ligands from Noble Metal Nanoparticles by Electrochemical Strategies. *ACS Catal.* **2018**, *8* (9), 8484−8492.

https://doi.org/10.1021/acscatal.3c06298
ACS Catal. 2024, 14, 5436−5443

(36) Xiang, W.; Yang, N.; Li, X.; Linnemann, J.; Hagemann, U.; Ruediger, O.; Heidelmann, M.; Falk, T.; Aramini, M.; DeBeer, S.; Muhler, M.; Tschulik, K.; Li, T. 3D atomic-scale imaging of mixed Co-Fe spinel oxide nanoparticles during oxygen evolution reaction. *Nat. Commun.* **2022**, *13* (1), 179.
(37) Lu, L.; Zou, S.; Zhou, Y.; Liu, J.; Li, R.; Xu, Z.; Xiao, L.; Fan, J. Ligand-regulated ORR activity of Au nanoparticles in alkaline medium: the importance of surface coverage of ligands. *Catal. Sci. Technol.* **2018**, *8* (3), 746−754.
(38) Omasta, T. J.; Peng, X.; Miller, H. A.; Vizza, F.; Wang, L.; Varcoe, J. R.; Dekel, D. R.; Mustain, W. E. Beyond 1.0 W cm^{-2} Performance without Platinum: The Beginning of a New Era in Anion Exchange Membrane Fuel Cells. *J. Electrochem. Soc.* **2018**, *165* (15), J3039.
(39) Entwistle, J.; Ge, R.; Pardikar, K.; Smith, R.; Cumming, D. Carbon binder domain networks and electrical conductivity in lithium-ion battery electrodes: A critical review. *Renewable and Sustainable Energy Reviews* **2022**, *166*, 112624.
(40) Dieterich, W.; Dürr, O.; Pendzig, P.; Bunde, A.; Nitzan, A. Percolation concepts in solid state ionics. *Physica A: Statistical Mechanics and its Applications* **1999**, *266* (1), 229−237.
(41) Bhargava, A.; Eppstein, R.; Sun, J.; Smeaton, M. A.; Paik, H.; Kourkoutis, L. F.; Schlom, D. G.; Caspary Toroker, M.; Robinson, R. D. Breakdown of the Small-Polaron Hopping Model in Higher-Order Spinels. *Adv. Mater.* **2020**, *32* (49), 2004490.
(42) Adabi, H.; Shakouri, A.; Ul Hassan, N.; Varcoe, J. R.; Zulevi, B.; Serov, A.; Regalbuto, J. R.; Mustain, W. E. High-performing commercial Fe−N−C cathode electrocatalyst for anion-exchange membrane fuel cells. *Nature Energy* **2021**, *6* (8), 834−843.

https://doi.org/10.1021/acscatal.3c06298
ACS Catal. 2024, 14, 5436−5443